JOURNAL OF THERMOPHYSICS AND HEAT TRANSFER
Vol. 10, No. 4, October–December 1996

Plasmadynamics Model for Nonequilibrium Processes in N_2/H_2 Arcjets

Thomas W. Megli,* Herman Krier,† and Rodney L. Burton‡
University of Illinois at Urbana–Champaign, Urbana, Illinois 61801

A two-temperature chemical nonequilibrium model is developed for nitrogen/hydrogen (N_2/H_2) arcjet thrusters. All viscous flow properties are considered assuming steady, laminar, continuum, and axisymmetric flow. A seven-species N_2/H_2 plasma composition of molecules, atoms, ions, and electrons is assumed, and a finite rate chemistry model is employed to model collisional processes among the species. Separate energy equations are formulated for the electrons and heavy species. The anode temperature distribution is included, and propellant electrical conductivity is coupled to the plasma properties, allowing for a self-consistent current distribution. The numerical solution employs the compressible form of the pressure-implicit with splitting of operators algorithm to solve the continuity and momentum equations. Numerical results are presented for a low-power simulated hydrazine thruster. The centerline constrictor region of the arcjet flowfield is predicted to be near thermal equilibrium, whereas a high degree of thermal nonequilibrium is predicted in the near-anode region of the arcjet nozzle. Strong electric fields near the anode produce elevated electron temperatures that enhance ionization levels and electrical conduction through the arcjet boundary layer. Radial diffusion of electrons from the arc core also enhances the near-anode ionization levels. Thus, the nonequilibrium approach is required to accurately model the plasma current distribution.

Nomenclature

C = coulomb charge
c_i = mean thermal speed, m/s
D_i = effective diffusion coefficient, m^2/s
d = diameter, m
$elst$ = elastic energy transfer, W/m^3
g_0 = gravitational acceleration at sea level, m/s^2
H = heavy species total particle energy, J
h = Planck's constant, J-s
h_i = enthalpy of species i, J/kg
I = integrated total current, A
I_{sp} = specific impulse, s
j = current density, A/m^2
k_b = Boltzmann's constant, J/K
k_c = coulomb constant, Nm^2/C^2
M = Mach number
$\dot{m}$ = mass flow rate, kg/s
m_i = mass of species i, kg
m_{ij} = reduced mass, kg
$\bar{n}$ = surface normal vector
n_i = number density of ith species, m^{-3}
P = electrical power, W
p = pressure, N/m^2
Q_{ij} = collision cross section, m^2
T = thrust, N
T_a = anode temperature, K
T_c = cathode temperature, K
T_e = electron temperature, K
T_g = heavy species temperature, K
u = axial velocity, m/s
V = voltage, V
v = radial velocity, m/s
$\boldsymbol{v}$ = velocity vector, m/s
w = azimuthal swirl velocity, m/s
x_i = mole fraction of species i
x_{mol} = mixture parameter in $x_{mol}\ N_2 + H_2$
x, r, θ = cylindrical coordinates
α = nozzle half-angle
α_i = catalytic recombination coefficient
δ = electron–molecule inelastic loss factor
ε = anode emissivity
ε_d = dissociation energy, J
ε_i = ionization energy, J
Λ_e = coulomb logarithm term
λ_a = anode thermal conductivity, W/m-K
λ_e = electron thermal conductivity, W/m-K
λ_h = heavy species thermal conductivity, W/m-K
μ = gas viscosity, kg/m-s
ν = collision frequency, s^{-1}
θ_{vH_2} = H_2 vibrational temperature, K
θ_{vN_2} = N_2 vibrational temperature, K
ρ = mass density, kg/m^3
σ = electrical conductivity, mho/m
τ = stress tensor, N/m^2
$\bar{\Omega}_{ij}$ = collision integral, m^2

Presented as Paper 95-1961 at the AIAA 26th Plasmadynamics and Lasers Conference, San Diego, CA, June 19–22, 1995; received Feb. 19, 1996; revision received June 10, 1996; accepted for publication June 10, 1996. This paper was selected for the 1995 Plasmadynamics and Lasers Best Paper Award.

*Ph.D. Candidate, Department of Mechanical and Industrial Engineering; currently at Ford Research and Engineering Center, 21500 Oakwood Boulevard, Dearborn, MI 48121. Member AIAA.

†Professor, Department of Mechanical and Industrial Engineering, 1206 West Green Street. Fellow AIAA.

‡Associate Professor, Department of Aeronautical and Astronautical Engineering, 104 South Wright Street. Associate Fellow AIAA.

Introduction

ELECTROTHERMAL arcjets offer a significant advantage in specific impulse and cost over conventional satellite propulsion systems. Low-power (1–2 kW) systems have been flight qualified and are now used for North–South station keeping, while higher power 20–30-kW designs are in advanced development for orbit transfer applications.[1]

The arcjet is shown schematically in Fig. 1. Injected $\dot{m}$ enters the constrictor and is ionized and heated by current flowing from anode to cathode. The propellant, typically injected upstream of the constrictor, is given an azimuthal (or swirl) velocity component. Propellant heating occurs in the arc dis-

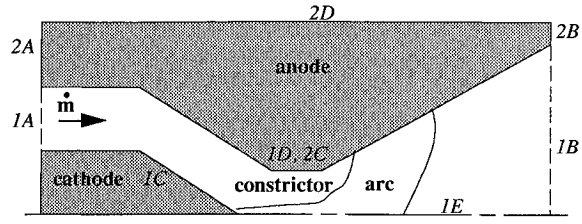

Fig. 1 Schematic of arcjet thruster indicating fluid and anode domain boundaries.

charge, produced by a voltage difference between the anode thruster nozzle and a conical cathode on the upstream side of the constrictor. The typical operating voltage for 1-kW class arcjet is 100 V dc at $I = 10$ A. The arc current distribution depends on several factors in addition to the geometry. The distribution is coupled to the propellant mass flow rate, composition, thermal properties, electrical conductivity, and gas-dynamic properties.

Both chemical and thermal processes in the arcjet are described as nonequilibrium. Arc current is converted to electron thermal energy through ohmic dissipation. The electrons transfer thermal energy to heavy species in the arc plasma through collisions. This energy is then converted to thrust as the fluid accelerates through the nozzle. In regions of low pressure and/or elevated ohmic heating, collisional coupling between electrons and heavy species may not establish equal gas and electron temperatures. Additionally, flow velocities are large so that fluid residence times in the nozzle are of the order of a few μs, and much of the energy invested in dissociation and ionization is frozen. Pressures drop from roughly 1 atm at the constrictor to millitorr conditions at the exit; radial diffusion of electrons from the arc core is important in determining the arc structure.

The thrust and specific impulse produced by an arcjet are determined by several factors, including the power transferred to the propellant, the extent of both thermal and chemical nonequilibrium, the propellant gas mixture, and the arcjet nozzle geometry. Other factors that contribute to the overall performance include the thermal loading of the anode[2] and the voltage sheaths at the electrodes. A comprehensive model of an arcjet thruster is highly complex, including plasmadynamic, fluid dynamic, radiative, and surface and volumetric heat transfer phenomena.

Most arcjet design strategies to date have been empirical, with design improvements based on experimental observations. The need for a more complete description of the complex physical processes has resulted in a variety of numerical efforts ranging from simplified one-dimensional models[3-8] to more comprehensive two-dimensional descriptions of the gas-dynamics and energy transfer processes.[9-22] Comprehensive arcjet models are required to 1) interpret experimental results, 2) understand the physical processes in regions of the thruster where diagnostic techniques are challenging, 3) improve arcjet performance, and 4) scale the devices to higher specific power levels.

Model

An axisymmetric, steady, laminar, continuum flow, two-temperature chemical nonequilibrium model is formulated for a direct current arcjet with flow swirl, a variable nozzle geometry, and a variable mixture ratio of nitrogen and hydrogen. Flow swirl is modeled by including an azimuthal momentum equation.

The model predicts thrust, specific impulse, and internal fields for p, ρ, seven-species n_i, and T_a, T_e, and T_g temperatures. Additionally, the model predicts the distribution j, V, and velocity components u, v, and w.

The details of the model are presented in six sections as the 1) fluid dynamic equations, 2) energy equations, 3) electromagnetic equations, 4) species number density equations, 5) transport coefficients, and 6) boundary conditions. The arcjet geometry is described as x, r, θ, where x is the axial coordinate, r is the radial coordinate, and θ is the azimuthal coordinate.

Fluid Dynamic Equations

The viscous fluid dynamic equations are summarized as follows:

Axial momentum

$$\frac{\partial(\rho uu)}{\partial x} + \frac{1}{r}\frac{\partial(r\rho uv)}{\partial r} = \frac{4}{3}\frac{\partial}{\partial x}\left(\mu\frac{\partial u}{\partial x}\right) + \frac{1}{r}\frac{\partial}{\partial r}\left(\mu r\frac{\partial u}{\partial r}\right) - \frac{2}{3}\frac{\partial}{\partial x}\left(\mu\frac{\partial v}{\partial r}\right) - \frac{2}{3r}\frac{\partial(\mu v)}{\partial x} + \frac{1}{r}\frac{\partial}{\partial r}\left(\mu r\frac{\partial v}{\partial x}\right) - \frac{\partial p}{\partial x} \quad (1)$$

Radial momentum

$$\frac{\partial(\rho uv)}{\partial x} + \frac{1}{r}\frac{\partial(r\rho vv)}{\partial r} = \frac{\partial}{\partial x}\left(\mu\frac{\partial v}{\partial x}\right) + \frac{4}{3r}\frac{\partial}{\partial r}\left(\mu r\frac{\partial v}{\partial r}\right) + \frac{\partial}{\partial x}\left(\mu\frac{\partial u}{\partial r}\right) + \frac{2\mu}{3r}\frac{\partial u}{\partial x} - \frac{2v}{3r}\frac{\partial\mu}{\partial r} - \frac{4}{3}\frac{\mu v}{r^2} - \frac{2}{3r}\frac{\partial}{\partial r}\left(\mu r\frac{\partial u}{\partial x}\right) - \frac{\partial p}{\partial r} + \frac{\rho w^2}{r} \quad (2)$$

Azimuthal momentum ($\partial p/\partial\theta = 0$)

$$\frac{\partial[\rho u(wr)]}{\partial x} + \frac{1}{r}\frac{\partial}{\partial r}[(r\rho v + 2\mu)(wr)] = \frac{\partial}{\partial x}\left[\mu\frac{\partial(wr)}{\partial x}\right] + \frac{1}{r}\frac{\partial}{\partial r}\left[\mu r\frac{\partial(wr)}{\partial r}\right] \quad (3)$$

Axisymmetric continuity

$$\frac{\partial}{\partial x}(\rho u) + \frac{1}{r}\cdot\frac{\partial}{\partial r}(r\rho v) = 0 \quad (4)$$

The variable p, appearing in Eqs. (1) and (2), is obtained from the two-temperature plasma equation of state:

$$p = n_e k_b T_e + (n_{N_2} + n_{H_2} + n_N + n_H + n_e)k_b T_g \quad (5)$$

Energy Equations

The assumption of thermal nonequilibrium requires separate energy equations for the electrons and heavy species. The electron energy equation is

$$\nabla\cdot[(n_e\boldsymbol{v} - (j/e)(C_{pe}T_e)] = \nabla\cdot(\lambda_e\nabla T_e) + \nabla\cdot[(1/m_e)\rho C_{pe}T_e D_e\nabla y_e] + (j\cdot j/\sigma) - elst - \text{radiation} - \sum L_e \quad (6)$$

where *elst* represents energy lost through elastic collisions with the heavy species,[23] and radiation denotes optically thin radiation because of the continuum bremsstrahlung.[24] The elastic energy transfer source term is calculated as the sum of electron–molecule, –atom, and –ion contributions as

$$elst = 3k_b(T_e - T_g)n_e m_e \sum_{i\neq e}\frac{\bar{\nu}_{ei}}{m_i} \quad (7)$$

where the average collision frequencies $\bar{\nu}_{ei}$ between electrons and heavy species are calculated using the mean electron thermal speed and collision cross sections Q_{es} as[24]

$$\bar{\nu}_{ei} = \sqrt{(8k_b T_e/\pi m_e)}n_i Q_{ei} \quad (8)$$

Table 1 Finite rate chemistry model

Reaction[a]	Rate, m^6/s or m^3/s	Loss rate, W/m^3	Reference
$2H + M = H_2 + M$	$k_{f1} = 1.764 \times 10^{-42}/T_g$	$L_h = \begin{bmatrix} k_{r1} n_{H_2} \\ -k_{f1} n_H^2 \end{bmatrix} n_M \varepsilon_{d,H_2}$	28
$H^+ + e + M = H + M$	$k_{f2} = 1.45 \times 10^{-33}/T_g^{2.5}$	$L_h = \begin{bmatrix} k_{r2} n_H \\ -k_{f2} n_{H^+} n_e \end{bmatrix} n_M \varepsilon_{i,H}$	28
$e + H_2 \rightarrow 2H + e$	$k_{f3} = \langle \sigma v \rangle$	$L_e = k_{f3} n_e n_{H_2} \varepsilon_{d,H_2}$	29
$H^+ + e \rightarrow H + h\nu$	$k_{f4} = 6.26 \times 10^{-17}/T_e^{0.58}$	$L_e = k_{f4} n_e n_{H^+} \varepsilon_{i,H}$	28
$H^+ + 2e = H + e$	$k_{f5} = 1.95 \times 10^{-20}/T_e^{4.5}$	$L_e = \begin{bmatrix} k_{r6} n_H \\ -k_{f6} n_e n_{H^+} \end{bmatrix} n_e \varepsilon_{i,H}$	28
$N_2 + M \rightarrow 2N + M$	$k_{f7} = (6.14 \times 10^{-9}/T_g^{1.6}) e^{-113{,}200/T_g}$	$L_h = k_{f7} n_{N_2} n_M \varepsilon_{d,N_2}$	30
$M + 2N \rightarrow N_2 + M$	$k_{f8} = (8.10 \times 10^{-37}/T_g^{1.39}) e^{1745/T_g}$	$L_h = -k_{f8} n_N^2 n_M \varepsilon_{d,N_2}$	30
$e + N_2 \rightarrow 2N + e$	$k_{f9} = (4.98 \times 10^{-6}/T_e^{1.6}) e^{-113{,}200/T_e}$	$L_e = k_{f9} n_e n_{N_2} \varepsilon_{d,N_2}$	31
$N + e = N^+ + 2e$	$k_{f10} = (4.15 \times 10^3/T_e^{3.82}) e^{-168{,}200/T_e}$	$L_e = \begin{bmatrix} k_{f10} n_N \\ -k_{r10} n_e n_{N^+} \end{bmatrix} n_e \varepsilon_{i,N}$	31

[a] $\rightarrow$, one way reactions; $=$, two way reactions with the reverse rate evaluated using the chemical equilibrium constants; M is any heavy species third body.

where the electron–ion cross sections are

$$Q_{e-\text{ion}} = \frac{\pi e^4 k_c^2 \ell n \Lambda_c}{2(k_b T_e)^2} \tag{9}$$

In Eq. (7), electron–molecule collision frequencies are multiplied by δ to account for inelastic losses to the internal modes.[8,25] Although this energy loss is generally electron temperature-dependent, a constant loss factor of $\delta = 3000$ is employed. The relatively high energy-independent value is chosen because of the following:

1) Significant uncertainties in δ are noted in the literature.[8]

2) Reasonable predictions for convective effects result, with the arc being swept further downstream as the mass flow rate is increased, as was originally postulated in Ref. 8.

3) Better agreement is achieved between the predicted and experimentally observed operating voltage, while maintaining the equipotential anode voltage boundary condition in the constrictor. This is further discussed in Refs. 26 and 27.

A finite rate chemistry model is used to determine the remaining inelastic energy exchange rates between the particle classes. These appear as ΣL_e in Eq. (6), and the model is summarized in Table 1, which lists the individual reaction rates and energy exchanges assumed for each chemical process.[28–31]

The heavy species energy equation is

$$\nabla \cdot (n_h \nu H) = \nabla \cdot (\lambda_h \nabla T_g) + \sum_{i \neq e} \frac{1}{m_i} \nabla \cdot [\rho (C_{pi} T_g + h_i^0) D_i \nabla y_i] + elst + \nabla \cdot (\nu \cdot \tau) - \sum L_h \tag{10}$$

where

$$H = \frac{1}{n_h} \sum_{i \neq e} \left[n_i \left(C_{pi} T_g + h_i^0 + \frac{m_i \nu \cdot \nu}{2} \right) \right] \tag{11}$$

The reference enthalpies h_i^0 and thermodynamic functions C_{pi} appearing in Eqs. (10) and (11) are listed in Table 2. The h_i^0 terms are the ground state vibrational energies for N_2 and H_2, whereas the C_{pi} include translational, rotational, and vibrational energy contributions. The inelastic exchange rates ΣL_h are summarized in Table 1.

The anode temperature distribution is determined from the energy equation for heat conduction in a solid. Neglecting ohmic dissipation in the anode gives

$$\nabla \cdot (\lambda_a \nabla T_a) = 0 \tag{12}$$

where $\lambda_a = \lambda_a(T_a)$.[32]

Table 2 Species reference enthalpies and thermodynamic functions C_p

Species	C_{pi}, J/K	h_i^0, J/particle
e	$\frac{5}{2} k_b$	0
H_2	$k_b[\frac{7}{2} + (\theta_{vH_2}/T_g)(e^{\theta_{vH_2}/T_g} - 1)^{-1}]$	$k_b/2\theta_{vH_2}$
N_2	$k_b[\frac{7}{2} + (\theta_{vN_2}/T_g)(e^{\theta_{vN_2}/T_g} - 1)^{-1}]$	$k_b/2\theta_{vN_2}$
H	$\frac{5}{2} k_b$	0
N	$\frac{5}{2} k_b$	0
H^+	$\frac{5}{2} k_b$	0
N^+	$\frac{5}{2} k_b$	0

Species Equations

The individual species continuity equations are written in terms of the species mass fractions $y_i = m_i n_i / \rho$:

$$\nabla \cdot (\rho \nu y_i) = \nabla \cdot (\rho D_i \nabla y_i) + \dot{\rho}_i \tag{13}$$

Mixture-averaged mass D_i are employed, rather than multicomponent diffusion coefficients. With this method, Eq. (13) is solved for y_{N_2}, y_H, y_N, y_{N^+}, and y_{H^+}. The electron population is then calculated from quasineutrality

$$n_e = n_{H^+} + n_{N^+} \tag{14}$$

and y_{H_2} is determined from overall mass continuity, or equivalently $\Sigma y_i = 1$. The species productions rates $\dot{\rho}_i = m_i \dot{n}_i$, are determined as a function of T_g and T_e from the finite rate chemistry processes summarized in Table 1. The references for the individual reaction rates are summarized in the right column of Table 1. For two-way reactions, the reverse reaction rates are extracted from the forward reaction rate and chemical equilibrium constants as determined from a generalized multitemperature law of mass action.[27]

Electromagnetic Equations

The calculation of the electrical current distribution is critical to understanding arc physics and poses a challenging problem in arcjet analysis. The current distribution is largely determined by the flowfield σ, which is a strong function of the electron number density and temperature distribution. Models that assume local thermodynamic equilibrium must artificially elevate σ in the cool boundary-layer region to avoid excessive voltage drops near the anode.[11,15] The artificial restriction that $T_e = T_g$ results in an underprediction in the ionization (and, therefore, electron number density and σ) in the boundary-layer regions and a subsequent overprediction in power deposition. Hence, the conductivity floor is employed elsewhere[10,14] to provide agreement between the experimentally observed and predicted power depositions.

Diffusion of electrons from the arc core toward the anode wall also elevates the electron number density and plays an important role in determining the boundary-layer electrical conductivity. This has been demonstrated by Butler et al.,[11] who show that the incorporation of mass diffusion provides a reasonable current distribution without imposing artificial restrictions on σ or the current attachment region. However, the two-temperature solutions of Miller and Martinez-Sanchez[17] and Keefer et al.[16] demonstrate that significant kinetic nonequilibrium, with elevated T_e, exists outside of the arc core in the constrictor region. These results indicate that both diffusion and increased ionization caused by elevated T_e are important factors that determine the boundary-layer electrical conductivity. Therefore, this investigation focuses on both thermal and chemical nonequilibrium aspects of arcjet flows.

The correct approach to the arc attachment problem is to model the anode as an equipotential surface and allow the current distribution to be a model output that is independent of artificial restrictions. This is a self-consistent approach to solving for the current distribution and electric field simultaneously, for which the current distribution is properly coupled to the flowfield.

Assuming induced magnetic fields are negligible, and neglecting electron pressure gradient driving terms, Ohm's law and current conservation are used to solve for j and V[25]:

$$-\nabla V = j/\sigma \tag{15}$$

$$\nabla \cdot j = 0 \tag{16}$$

Transport Coefficients

Transport coefficients are calculated using mean free path mixture rules.[33] The viscosity is computed as

$$\mu = \sum_{i=1}^{N} \left(n_i \Big/ \sum_{j=1}^{N} n_j M_{ij} \right) \mu_i \tag{17}$$

where M_{ij} is defined as

$$M_{ij} = \sqrt{(2m_{ij}/m_i)}[\bar{\Omega}_{ij}^{(2,2)}/\bar{\Omega}_{ii}^{(2,2)}] \tag{18}$$

and the pure species viscosity is

$$\mu_i = \tfrac{1}{2} m_i n_i c_i l_i \tag{19}$$

where l_i is the mean free path, and $\bar{\Omega}_{ij}$ is the energy-averaged integral for interaction between species i and j.

The translational contribution to the heavy species thermal conductivity is calculated using an expression similar to Eq. (17), with the pure species conductivity given as

$$\lambda_i = \frac{15}{8} k_b n_i c_i l_i \left(\frac{9\gamma_i - 5}{15\gamma_i - 15} \right) \tag{20}$$

The electron thermal conductivity is

$$\lambda_e = \frac{15}{8} k_b n_e^2 c_e l_e \left(\frac{9\gamma_e - 5}{15\gamma_e - 15} \right) \Big/ \sum_{j=1}^{N} n_j M_{ij} \tag{21}$$

and electrical conductivity is calculated from

$$\sigma = n_e e^2 \Big/ m_e \sum_{i \neq e} n_i c_e \bar{\Omega}_{e-i}^{(1,1)} \tag{22}$$

The D_i are calculated from

$$D_i = (1 - x_i) \Big/ \sum_{j \neq i} x_j / D_{ij} \tag{23}$$

where the D_{ij} are the binary mixture diffusion coefficients given as[34]

$$D_{ij} = \frac{3}{16 n \bar{\Omega}_{ij}^{(1,1)}} \left[\frac{2k_b T(m_i + m_j)}{\pi m_i m_j} \right]^{1/2} \tag{24}$$

The electron and ion diffusion coefficients are modified to account for the ambipolar electric field. Assuming $\nabla(n_e/\rho)/n_e \approx \nabla(n_{H^+}/\rho)/n_{H^+} \approx \nabla(n_{N^+}/\rho)/n_{N^+}$, the ambipolar diffusion coefficients for electrons, H^+, and N^+ are

$$D_{a,e} = \frac{D_e(\mu_{H^+} n_{H^+} + \mu_{N^+} n_{N^+}) + \mu_e(D_{H^+} n_{H^+} + D_{N^+} n_{N^+})}{\mu_e n_e + \mu_{H^+} n_{H^+} + \mu_{N^+} n_{N^+}} \tag{25}$$

$$D_{a,H^+} = \frac{D_{H^+}(\mu_e n_e + \mu_{N^+} n_{N^+}) + \mu_{H^+}(D_e n_e - D_{N^+} n_{N^+})}{\mu_e n_e + \mu_{H^+} n_{H^+} + \mu_{N^+} n_{N^+}} \tag{26}$$

$$D_{a,N^+} = \frac{D_{N^+}(\mu_e n_e + \mu_{H^+} n_{H^+}) + \mu_{N^+}(D_e n_e - D_{H^+} n_{H^+})}{\mu_e n_e + \mu_{H^+} n_{H^+} + \mu_{N^+} n_{N^+}} \tag{27}$$

where the mobilities μ are calculated from $\mu_i = eD_i/k_b T_i$.

The previous relations require the energy-averaged collision integrals for 28 species interactions. Collision integrals and collision cross sections are obtained from Refs. 35–41. Temperature-dependent curve fits are used for the transport property and elastic transfer calculations.

Boundary Conditions

The physical boundary conditions for the continuity, momentum, energy, and electromagnetic equations are summarized in Table 3 and Fig. 1. At the inflow boundary 1A, the flow is axial and the total temperature T_t and total pressure p_t are specified. The total pressure is adjusted to obtain the desired mass flow rate. The u velocities and the inlet static temperatures are then computed from the isentropic stagnation property relations. The effects of flow swirl are incorporated by specifying the azimuthal inlet w velocities as a fraction of the u velocities. At the solid cathode 1C and anode 1D surfaces, no-slip conditions are employed. Zero radial gradients are specified on the centerline 1E.

At the outflow boundary 1B, the static pressure is extrapolated from the interior of the flow. This is reasonable since the solutions indicate supersonic flow over the majority of the exit plane, with the subsonic region being confined to a thin annular region near the nozzle wall. The outflow u velocities are updated to satisfy continuity using velocity corrections as given by discretized forms of the momentum and continuity equations for the exit plane. This is consistent with the numerical solution method discussed later. A zero radial electron temperature gradient is employed at the walls 1C and 1D, effectively insulating the electrons from the solid surfaces.[42] This provides more physically accurate transport coefficient estimates, based on elevated electron temperatures and ionization levels, at the plasma/anode interface.

The boundary conditions for the voltage are shown in Table 3. The anode is modeled as an equipotential surface, whereas the cathode voltage is equipotential with the voltage updated to obtain the specified I. The axial gradient of the voltage is set to zero at the inflow and outflow boundaries so that current is forced to attach within the arcjet nozzle.

The assumption of quasineutrality is not valid very near plasma electrode surfaces. The thickness of this sheath region is of the order of the Debye length, which is typically much smaller than the characteristic lengths for temperature and ve-

Table 3 Boundary conditions for the fluid dynamic, energy, and electromagnetic equations[a]

Flowfield domain					
Variable	1A	1B	1C	1D	1E
u	From stagnation properties	From momentum	=0	=0	$\frac{\partial u}{\partial r} = 0$
v	=0	Extrapolated	=0	=0	=0
w	Specified	Extrapolated	=0	=0	=0
T_e	$\frac{\partial T_e}{\partial x} = 0$	Extrapolated	$\frac{\partial T_e}{\partial r} = 0$	$\frac{\partial T_e}{\partial r} = 0$	$\frac{\partial T_e}{\partial r} = 0$
T_g	From M and T_t	Extrapolated	Specified $T_g(x)$	$T_g = T_a$	$\frac{\partial T_g}{\partial r} = 0$
P	Extrapolated	Extrapolated	$\frac{\partial P}{\partial \bar{n}} = 0$	$\frac{\partial P}{\partial \bar{n}} = 0$	$\frac{\partial P}{\partial r} = 0$
V	$\frac{\partial V}{\partial x} = 0$	$\frac{\partial V}{\partial x} = 0$	$V = V_{cat}$	$V_s = 13$ V	$\frac{\partial V}{\partial r} = 0$

Anode domain				
Variable	2A	2B	2C	2D
T_a	$T_a = 1000$ K	$\dot{q} = \varepsilon\sigma(T_s^4 - T_{bg}^4)$	$\dot{q} = \lambda_h \frac{\partial T_g}{\partial \bar{n}} + \lvert j \rvert \left(V_s + \frac{5}{2e} k_b T_e \right) - \sum_{i=1}^{N} \frac{1}{m_i} \rho (C_{pi} T_i + h_i^0) D_i \frac{\partial y_i}{\partial \bar{n}} - \varepsilon \sin \alpha \sigma (T_s^4 - T_{bg}^4)$	$\dot{q} = \varepsilon\sigma(T_s^4 - T_{bg}^4)$

[a]Energy equation boundary conditions are shown for both the fluid and anode domains. For radiative boundary conditions, T_s is the local anode surface temperature.

locity changes. Net space charge creates electric fields in this region, which are large compared to those in the bulk plasma. Therefore, large voltage drops and power losses may occur. In this study, the electric fields in the sheath regions are treated as a fixed boundary condition, with an assumed anode sheath voltage fall of $V_s = 13.0$ V. This value, which was chosen based on cathode fall voltage estimates for high-pressure arcs[43] and estimates for the anode fall voltage from simple collisionless sheath theory,[27] is generally conservative in terms of the anode thermal loading.

The boundary conditions for the anode energy equation are also shown in Table 3. On the outer surfaces 2B and 2D, the local heat flux is given by radiation to the surroundings at a specified background temperature $T_{bg} << T_a$ and a constant emissivity of $\varepsilon = 0.31$, which is reasonable for tungsten.[12] Along the anode surface 2C, the net heat flux is a balance between 1) conduction and species diffusion heat fluxes to and from the flowfield, 2) the anode surface radiation loss through the exit plane to the surroundings, 3) the sheath losses given by the product of the local current density and an assumed sheath voltage drop $V_s = 13$ V, and 4) the electron current enthalpy flux. Numerical solutions indicate that the optically thin plasma radiation loss term is less than 1% of the total electrical power input; therefore, radiation exchange between the plasma volume and the anode surface is neglected in this formulation. The upstream anode surface 2A is either a fixed temperature or zero heat flux boundary.

Boundary conditions are required for the species populations. At the anode surface, the diffusion velocities are equated to a fraction α_i of the species thermal velocities[31]:

$$D_i \frac{\partial y_i}{\partial \bar{n}} = \frac{\alpha_i}{4} \sqrt{\frac{8 k_b T_g}{\pi m_i}} \tag{28}$$

The anode is assumed to be catalytic for recombination, so that $\alpha_{H^+} = \alpha_{N^+} = \alpha_H = \alpha_N = 1$. Assuming that molecules are reflected from the surface gives $\alpha_{H_2} = \alpha_{N_2} = 0$. The mass fractions at the exit plane are extrapolated from the interior of the flow.

The inflow is assumed to be in chemical equilibrium up to the constrictor entrance, where the chemical nonequilibrium simulation begins. In the chemical equilibrium inflow, the following relation, derived from an overall species balance, is enforced:

$$x_{mol} = \frac{2n_{N_2} + n_N + n_{N^+}}{2n_{H_2} + n_H + n_{H^+}} \tag{29}$$

where the initial mixture composition is written as $x_{mol}\ N_2 + H_2$, so that pure hydrogen ($x_{mol} = 0$), simulated hydrazine ($x_{mol} = \frac{1}{2}$), and simulated ammonia ($x_{mol} = \frac{1}{3}$) can be easily investigated. The relative species densities in the inflow region are determined from two-temperature equilibrium constants, as discussed in Ref. 27.

Numerical Solution Method

The solution method is structured around the global continuity and momentum equations. These are solved using a compressible form of the pressure-based pressure-implicit with splitting of operator algorithm,[44] where the density variations are implicitly included in the pressure-correction procedure as described by Rhie.[45] Staggered velocity and scalar grids yield a well-connected pressure field. Upstream weighted densities are employed to ensure numerical stability.[46] The governing equations are transformed into natural coordinates and solved on a uniform computational mesh. The equations are discretized over finite cell volumes, and power-law differencing of convective and diffusive portions of the linearized coefficients preserves numerical stability in regions of the flow where convection dominates. The solution process is iterative, and values for the field variables from the latest iteration are used to linearize the source terms. Underrelaxation is employed so that updated solutions are fractionally added to the solution from the previous iteration.

The energy equations are solved to update heavy species-, electron-, and anode-temperature fields. The species number densities, transport coefficients, and source terms are then updated using the latest available temperatures and pressures. The continuity and momentum equations are solved to update the pressure and velocity fields. Finally, the voltage and current density distributions are updated. Iterations are continued until 1) the normalized energy equation residuals are within 1% of the electrical power input, 2) the difference between the inlet and exit plane mass flow rates is less than 1% of the total mass

flow rate, and 3) the axial and radial momentum equation residuals are within 1% of their respective exit momentum fluxes. Further details of the solution methodology can be found in Ref. 27.

Results and Discussion

Results are presented for the geometry of a NASA Lewis Research Center 1-kW arcjet operating on simulated hydrazine ($x_{mol} = 0.5$).[47] The arcjet constrictor is $x = 0.25$ mm long with a diameter of $d = 0.62$ mm. The nozzle has a half-angle of 20 deg and an area ratio of 225:1. The cathode gap spacing, as measured axially from the converging portion of the anode surface, is $x = 1.02$ mm. The upstream anode surface 2A (Fig. 1) temperature is constant at $T_a = 1000$ K, which is consistent with infrared pyrometry measurements of the exterior anode surface. The cathode 1C temperature varies linearly from $T_c = 1000$ K at the inlet to $T_c = 3000$ K at the cathode tip. The choice for the T_c agrees reasonably with experimental estimates based on emission spectroscopy measurements[48] and posttest observations that indicate the presence of a molten crater at the tip.[47] The inlet flow swirl velocity is 30% of the axial inflow velocity, and the inlet total temperature is $T_t = 1000$ K.

The computational grids, shown in Fig. 2, are comprised of 62 axial by 17 radial nodes for the plasma, and 62 axial by 9 radial nodes for the anode domain. Numerical accuracy was investigated by examining the solutions for several of the field variables on both coarse and fine grids. Studies of the temperatures, axial velocity, and electron number density fields indicate typical fractional error estimates of roughly 5–10%, based on Richardson extrapolation.[49] The fractional error estimate for the voltage is 5%. Simulation run time is roughly 20 h on a Convex C240 mainframe computer.

The global performance parameters for the simulation are summarized in Table 4. The propellant is hydrazine operating at $\dot{m} = 50.2$ mg/s and $I = 10$ A. The predicted voltage is $V = 87$ V, and the specific impulse is $I_{sp} = 440$ s. The voltage prediction is lower than experimental measurements, whereas the I_{sp} prediction is higher. Curran and Haag[47] measured $V \approx 120$ V and $I_{sp} \approx 435$ s at $\dot{m} = 49.7$ mg/s and $I = 10$ A. The underprediction in voltage may be because of neglect of the electron pressure gradient term in Ohm's law, and to deficiencies in modeling the cathode erosion, electrode sheath physics, and the inelastic energy exchange between the electrons and heavy species.

Table 4 Summary of input parameters and model predictions

Propellant, N_2H_4
Mass flow rate, 50.2 mg/s
Arc current, 10 A
Terminal voltage, 87.0 V
Thrust, 0.22 N
Specific impulse, 440 s

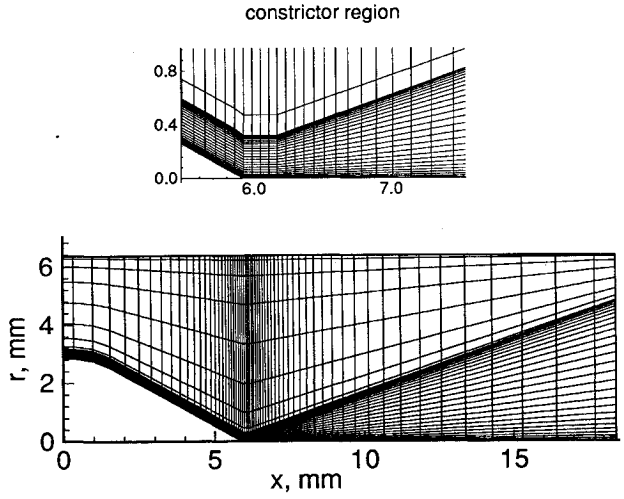

Fig. 2 Computational grids: the grids are tuned axially for high density in the constrictor and radially for high density near the electrode surfaces.

Contours of current density and anode temperature are indicated in Fig. 3. In the constrictor, the current is conducted in a region of ~100 μm diam, resulting in a centerline current density of $j \approx 70{,}000$ A/cm^2. The peak self-induced magnetic field is $B_\theta \approx 0.04$ T, justifying the assumed neglect of the magnetic pressure compared to the gasdynamic pressure.

Further downstream, the arc becomes more diffuse and attaches to the nozzle wall. A peak anode attachment current density of $j \approx 15$ A/cm^2 is noted at a location of $x \approx 8$ mm, or roughly 2 mm downstream of the constrictor. The anode temperature increases from the upstream boundary value of $T_a = 1000$ K to $T_a \approx 1200$ K near the exit plane. Approximately 266 W of power is transferred from the plasma to the anode, primarily because of sheath and thermal conduction losses. This is roughly 24% of the sum of the electrical power input ($P = 870$ W) and the upstream boundary inflow enthalpy (253 W).

Heavy species and electron temperature contours in the constrictor region are indicated in Figs. 4 and 5. In Fig. 4, a max-

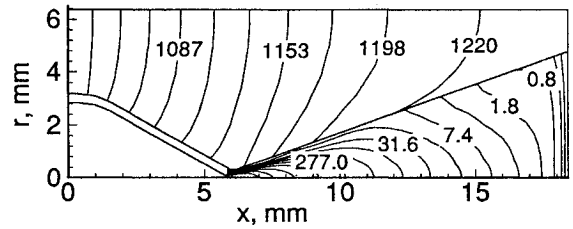

Fig. 3 Anode temperature and current density for hydrazine. The maximum anode current density is $j \approx 15$ A/cm^2 at $x \approx 8$ mm. The anode temperature increases from $T_a \approx 1000$ K at the upstream surface to $T_a \approx 1200$ K near the exit plane.

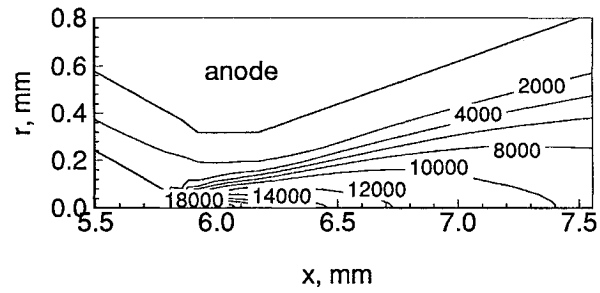

Fig. 4 T_g contours in the constrictor region. The maximum is $T_g \approx 20{,}000$ K at the constrictor centerline. The exit plane is located at $x = 18.4$ mm.

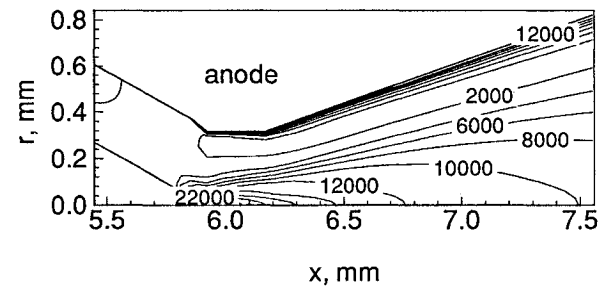

Fig. 5 T_e contours in the constrictor region. The maximum is $T_e \approx 25{,}000$ K at the constrictor centerline. The exit plane is located at $x = 18.4$ mm.

imum of $T_g \approx 22{,}000$ K occurs near the center of the constrictor. In the constrictor, the central region of the arc is near thermal equilibrium, as indicated by a similar maximum of $T_e \approx 28{,}000$ K shown in Fig. 5. The outer region of the flow exhibits a high degree of thermal nonequilibrium, caused by the intense ohmic heating of the electrons. This is shown in Fig. 5 where, at an axial location of $x \approx 7.5$ mm, the electron temperature decreases radially from a centerline value of $T_e \approx 10{,}000$ K, eventually reaching a minimum of $T_e \approx 2000$ K at a radial location of $r \approx 0.6$ mm. The electron temperature then increases to $T_e \approx 12{,}500$ K near the anode surface. From Figs. 3 and 4, the anode and heavy species temperatures are $T_a \approx T_g \approx 1100$ K in this region, which indicates a temperature ratio of $T_e/T_g \approx 11$. The thermal nonequilibrium indicated near the anode is qualitatively similar to the predictions of other nonequilibrium hydrogen arcjet models.[16,17] The elevated electron temperatures enhance ionization levels and allow current conduction through the cold gas layer near the nozzle wall. Radial outward diffusion of electrons from the hot, highly ionized arc core also enhances electrical conduction in the near-anode layer.

Axial velocity contours are shown in Fig. 6. A maximum centerline velocity of $u \approx 7$ km/s occurs at $x = 9$ mm, and then decreases near the constrictor exit because of intense arc heating. The velocity at the exit plane is $u \approx 6.5$ km/s. Although the centerline flow u velocity decreases, the nozzle produces axial acceleration over the entire length in the cooler outer flow region. The arc displaces the majority of the mass and momentum fluxes toward this outer region, because of the high radial gradients in heavy species temperature. The nozzle performance is largely determined by the acceleration of the high mass density outer flow region, rather than the deceleration of the low-density, high-temperature central flow. This suggests that performance benefits would be available from higher area ratio nozzles.

Model predictions are compared with experimental temperature measurements in Fig. 7. Nozzle centerline predictions for electron T_e and heavy species T_g temperatures are compared with internal emission spectroscopy measurements of excitational, vibrational, and rotational temperatures.[50] Electrostatic probe measurements for electron and ion translational temperatures downstream of the exit plane ($x = 18.4$ mm) are also indicated.[51] Model predictions for T_g are in good agreement with the N_2 vibrational and rotational temperature measurements, indicating that these temperatures may be roughly in equilibrium with the heavy species translational temperatures. The exit plane prediction of $T_g \approx 2500$ K also agrees well with the plume measurements for ion temperature. Interestingly, the model predicts $T_e \approx T_g$ on the centerline, while experimental measurements suggest $T_e/T_g \approx 2$–3. The disagreement may indicate the need for a more detailed description of the inelastic energy exchange rates between the electrons and heavy species. Also, the elevated T_e may indicate that the actual electric field in the downstream portion of the nozzle is stronger than that predicted by the model. A longer arc path would increase the ohmic heating and elevate electron temperatures, and may also explain discrepancies between the experimentally measured and predicted voltage. The experimentally observed thermal nonequilibrium clearly illustrates the need for at least two energy equations to accurately model the arcjet plasma flowfield.

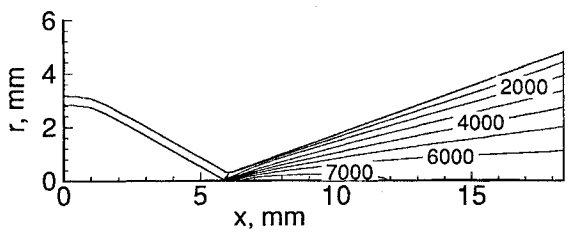

Fig. 6 Axial u-velocity contours. The maximum is $u \approx 7$ km/s at $x \approx 9$ mm. The centerline velocity decreases to $u \approx 6.5$ km/s at the exit plane.

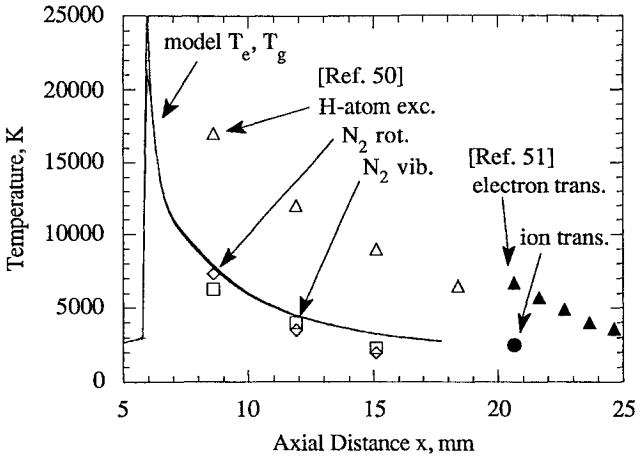

Fig. 7 Comparison of T_e and T_g temperature predictions with experimental measurements.[50,51]

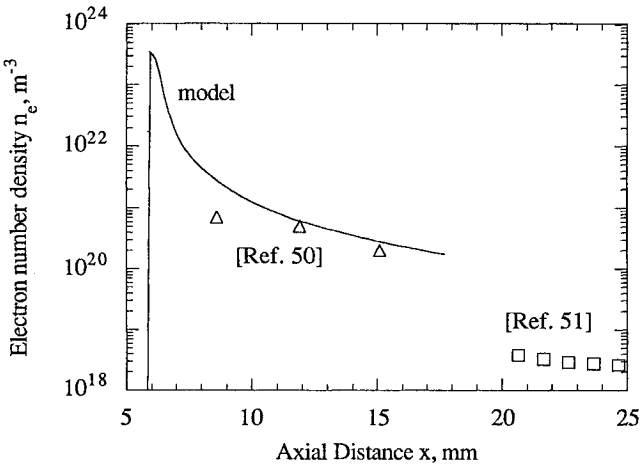

Fig. 8 Comparison of n_e predictions with experimental measurements.[50,51]

Centerline predictions for electron number density n_e are compared with the experiment in Fig. 8.[50,51] Model predictions for the interior nozzle region agree reasonably well with the experiment. The near-exit plane measurements of $n_e \approx 10^{18}$–10^{19} m^{-3} are significantly lower than the model exit-plane prediction of $n_e \approx 10^{20}$ m^{-3}. Radial expansion of the plume is likely responsible for the difference between the model and experiment. Thus, a valid comparison would require the extension of the model domain beyond the exit plane. This would require a noncontinuum approach, and is considered to be beyond the scope of the present research. The agreement between predicted and measured electron densities suggests that the finite rate chemistry model reasonably captures the electron–ion recombination phenomena in the interior of the nozzle.

Summary and Conclusions

A nonequilibrium model is formulated for N_2/H_2 arcjets. In this approach, a modified set of Navier–Stokes equations is employed, with separate energy equations to determine electron and heavy species temperatures. Species continuity equations are solved in conjunction with a finite rate chemistry model to determine inelastic energy exchange rates and species distributions.

Results for the 1-kW NASA Lewis Research Center thruster indicated a high degree of thermal nonequilibrium in the volt-

age fall region near the nozzle wall, with $T_e/T_g \approx 11$ predicted at the location of maximum anode current density. This nonequilibrium is a primary mechanism for maintaining the ionization levels required for electrical conduction through the cool near-electrode regions of the flow.

The model was compared with experimental measurements. Centerline heavy species temperature predictions agree favorably with measurements of N_2 rotational and vibrational temperatures, and estimates for the translational ion temperature in the near plume. Additionally, model predictions for electron density agree favorably with experimental measurements. Model predictions for centerline electron temperatures are in disagreement with experiment. A more complete description of the inelastic energy exchange rates between the electrons and heavy species may be required to resolve discrepancies between theory and experiment.

Acknowledgments

This work is funded by the U.S. Air Force Office of Scientific Research under Contracts F49620-92-J-0448 and -0280; Mitat Birkan is the Program Manager. The authors acknowledge stimulating dialogues with S. Bufton, N. Tiliakos, and G. Willmes. We thank S. P. Vanka and K. Cope for their advice on solving the energy equation in strong conservative form, and M. J. Kushner for helpful advice in constructing the model. We also thank J. Lu for assistance with the simulations and preparation of figures.

References

[1]Wilbur P. J., Jahn, R. G., and Curran, F. C., "Space Electric Propulsion Plasmas," *IEEE Transactions on Plasma Science*, Vol. 19, No. 6, 1991, pp. 1167–1179.

[2]Butler, G. W., Cassady, R. J., and King, D. Q., "Directions for Arcjet Technology Development," AIAA Paper 94-2652, June 1994.

[3]Jack, J. R., "Theoretical Performance of Propellants Suitable for Electrothermal Jet Engines," *ARS Journal*, Vol. 31, No. 12, 1961, p. 1685.

[4]John, R. R., Benett, S., Coss, L. A., Chen, M. M., and Connors, J. F., "Energy Addition and Loss Mechanisms in the Thermal Arcjet Engine," AIAA Paper 63-022, March 1963.

[5]Topham, D. R., "The Electric Arc in a Constant Pressure Axial Gas Flow," *Journal of Physics D: Applied Physics*, Vol. 4, No. 8, 1971, pp. 1114–1125.

[6]Glocker, B., Schrade, H. O., and Auweter-Kurtz, M., "Performance Calculation of Arcjet Thrusters: The Three Channel Model," IEPC Paper 93-187, Sept. 1993.

[7]Martinez-Sanchez, M., and Sakamoto, A., "Simplified Analysis of Arcjet Thrusters," AIAA Paper 93-1904, June 1993.

[8]Martinez-Sanchez, M., "Arcjet Modeling: Status and Prospects," AIAA Paper 94-2653, June 1994.

[9]Butler, G. W., Kashiwa, B. A., and King, D. Q., "Numerical Modeling of Arcjet Performance," AIAA Paper 90-1474, June 1990.

[10]Butler, G. W., and King, D. Q., "Single and Two Fluid Simulations of Arcjet Performance," AIAA Paper 92-3104, July 1992.

[11]Butler, G. W., Kull, A. E., and King, D. Q., "Numerical Simulations of Hydrogen Arcjet Performance," IEPC Paper 93-249, Sept. 1993.

[12]Butler, G. W., Kull, A. E., and King, D. Q., "Single Fluid Simulations of Low Power Hydrogen Arcjets," AIAA Paper 94-2870, June 1994.

[13]Rhodes, R., and Keefer, D., "Numerical Modeling of an Arcjet Thruster," AIAA Paper 90-2614, June 1990.

[14]Rhodes, R., and Keefer, D., "Modeling Arcjet Space Thrusters," AIAA Paper 91-1994, June 1991.

[15]Rhodes, R., and Keefer, D., "Non-Equilibrium Modeling of Hydrogen Arcjet Thrusters," IEPC Paper 93-217, Sept. 1993.

[16]Keefer, D., Burtner, D., Moeller, T., and Rhodes, R., "Multiplexed Laser Induced Fluorescence and Non-Equilibrium Processes in Arcjets," AIAA Paper 94-2656, June 1994.

[17]Miller, S., and Martinez-Sanchez, M., "Nonequilibrium Numerical Simulation of Radiation-Cooled Arcjet Thrusters," IEPC Paper 93-218, 1993; also "Two Fluid Nonequilibrium Simulation of Hydrogen Arcjet Thrusters," *Journal of Propulsion and Power*, Vol. 12, No. 1, 1996, pp. 112–119.

[18]Flowe, A. C., DeWitt, K. J., Keith, T. G., Jr., Pawlas, G. E., and Penko, P. F., "Numerical Modeling of Fluid and Electromagnetic Phenomena in an Arcjet," AIAA Paper 92-3106, July 1992.

[19]Ciucci, A., D'Agostino, L., and Andrenucci, M., "Development of a Numerical Model of the Nozzle Flow in Low Power Arcjet Thrusters," IEPC Paper 93-182, Sept. 1993.

[20]Fujita, K., and Arakawa, Y., "Anode Heat Loss and Current Distributions of DC Arcjets," IEPC Paper 93-185, Sept. 1993.

[21]Babu, V., Aithal, S., and Subramaniam, V. V., "On the Effects of Swirl in Arcjet Thruster Flows," IEPC Paper 93-183, Sept. 1993.

[22]Babu, V., Aithal, S., and Subramaniam, V. V., "Vibrational Non-Equilibrium in Arcjet Flows," IEPC Paper 93-129, Sept. 1993.

[23]Kruger, C. H., and Mitchner, M., "Kinetic Theory of Two Temperature Plasmas," *Physics of Fluids*, Vol. 10, No. 9, 1967, pp. 1953–1961.

[24]Mertogul, A. E., "Modeling and Experimental Measurements of Laser Sustained Plasmas," Ph.D. Dissertation, Dept. of Mechanical and Industrial Engineering, Univ. of Illinois, Urbana, IL, 1993.

[25]Sutton, G. W., and Sherman, A., *Engineering Magneto-Hydrodynamics*, McGraw–Hill, New York, 1965, pp. 148–190.

[26]Megli, T. W., Krier, H., and Burton, R. L., "A Plasmadynamics Model for Nonequilibrium Processes in N_2/H_2 Arcjets," AIAA Paper 95-1961, July 1995.

[27]Megli, T. W., "A Nonequilibrium Plasmadynamics Model for Nitrogen/Hydrogen Arcjets," Ph.D. Dissertation, Dept. of Mechanical and Industrial Engineering, Univ. of Illinois, Urbana, IL, 1995.

[28]McCay, D. T., and Dexter C. E., "Chemical Kinetic Performance Losses for a Hydrogen Laser Thermal Thruster," *Journal of Spacecraft*, Vol. 24, No. 4, 1987, pp. 372–376.

[29]Janev, R. K., Langer, W. D., Evans, K., Jr., and Post, D. E., Jr., *Elementary Processes in Hydrogen Helium Plasmas*, Springer–Verlag, New York, 1987.

[30]Cambier, J.-L., and Moreau, S., "Simulations of a Molecular Plasma in Collisional-Radiative Nonequilibrium," AIAA Paper 93-3196, June 1993.

[31]Park, C., *Nonequilibrium Hypersonic Aerothermodynamics*, Wiley, New York, 1990.

[32]Incropera, F. P., and Dewitt, D. P., *Fundamentals of Heat and Mass Transfer*, Wiley, New York, 1981, p. 758.

[33]Mitchner, M., and Kruger, C., *Partially Ionized Gases*, Wiley, New York, 1973.

[34]Maitland, G. C., Rigby, M., Smith, B. E., and Wakeham, W. A., *Intermolecular Forces*, Clarendon, Oxford, England, UK, 1981, p. 302.

[35]Capecchi, G., and D'Agostino, L., "Numerical Model of Equilibrium Composition and Transport Coefficients of Hydrazine Under Dissociation and Ionization," AIAA Paper 94-2868, June 1994.

[36]Stallcop, J. R., Partridge, H., and Levin, E., "Resonance Charge Transfer, Transport Cross Sections, and Collision Integrals for $N^+(^3P)$-$N(^4S^0)$ and $O^+(^4S^0)$-$O(^3P)$ Interactions," *Journal of Chemical Physics*, Vol. 95, No. 9, 1991, pp. 6429–6439.

[37]Stallcop, J. R., Bauschlicher, C. W., Partridge, H., and Levin, E., "Theoretical Study of Hydrogen and Nitrogen Interactions: N-H Transport Cross Sections and Collision Integrals," *Journal of Chemical Physics*, Vol. 97, No. 8, 1992, pp. 5578–5585.

[38]Levin, E., Partridge, H., and Stallcop, J. R., "Collision Integrals and High Temperature Transport Properties for N-N, O-O, and N-O," *Journal of Thermophysics and Heat Transfer*, Vol. 4, No. 4, 1990, pp. 469–477.

[39]Vanderslice, J. T., Weissman, S., Mason, E. A., and Fallon, R. J., "High Temperature Transport Properties of Dissociating Hydrogen," *Physics of Fluids*, Vol. 5, No. 2, 1962, pp. 155–164.

[40]Stallcop, J. R., Partridge, H., Walch, S. P., and Levin, E., "H–N_2 Interaction Energies, Transport Cross Sections, and Collision Integrals," *Journal of Chemical Physics*, Vol. 97, No. 5, 1992, pp. 3431–3436.

[41]Grier, N. T., "Calculation of Transport Properties of Ionizing Atomic Hydrogen," NASA TN D-1386, April 1966.

[42]Chang, C. H., and Pfender, E., "Nonequilibrium Modeling of Low Pressure Argon Plasma Jets; Part I: Laminar Flow," *Plasma Chemistry and Plasma Processing*, Vol. 10, No. 3, 1990, pp. 473–491.

[43]Goodfellow, K. D., "Theoretical Investigation of Cathode Operation in High-Power Arcjets," AIAA Paper 95-3061, July 1995.

[44]Issa, R. I., "Solution of the Implicitly Discretised Fluid Flow Equations by Operator-Splitting," *Journal of Computational Physics*, Vol. 62, No. 1, 1986, pp. 40–65.

[45]Rhie, C. M., "A Pressure-Based Navier Stokes Solver Using the Multigrid Method," AIAA Paper 86-0207, Jan. 1986.

[46]Karki, K. C., *A Calculation Procedure for Viscous Flows at All*

Speeds in Complex Geometries, Ph.D. Dissertation, Univ. of Minnesota, Bloomington, MN, 1986.

[47]Curran, F. M., and Haag, T. W., "Extended Life and Performance Test of a Low-Power Arcjet," *Journal of Spacecraft and Rockets*, Vol. 29, No. 4, 1992, pp. 444–452.

[48]Cappelli, M. A., and Storm, P. V., "Interior Plasma Diagnostics of Arcjet Thrusters," AIAA Paper 94-2654, June 1994.

[49]Roache, P. J., "A Method for Uniform Reporting of Grid Refinement Studies," Symposium on Quantification of Uncertainty in Computational Fluid Dynamics, American Society of Mechanical Engineers, Fluids Engineering Division Summer Meeting, Washington, DC, June 1993.

[50]Zube, D. M., and Myers, R. M., "Thermal Nonequilibrium in a Low-Power Arcjet Nozzle," *Journal of Propulsion and Power*, Vol. 9, No. 4, 1993, pp. 545–552.

[51]Bufton, S. A., Burton, R. L., and Krier, H., "Measured Plasma Properties at the Exit Plane of a 1 kW Arcjet," AIAA Paper 95-3066, July 1995.